Kinetically Controlled Morphology in Copolymer-based Hydrogels Crosslinked by Crystalline Nanodomains Determines Efficacy of Ice Inhibition

Journal:	*Molecular Systems Design & Engineering*
Manuscript ID	ME-ART-08-2019-000101.R1
Article Type:	Paper
Date Submitted by the Author:	20-Sep-2019
Complete List of Authors:	Sepulveda-Medina, Pablo; University of Akron, Polymer Engineering Wang, Chao; University of Akron, Polymer Engineering Li, Ruipeng; Cornell University, CHESS Fukuto, Masafumi; Brookhaven National Laboratory, Condensed Matter Physics and Materials Science Department Weiss, Robert; University of Akron, Department of Polymer Engineering Vogt, Bryan; University of Akron, Polymer Engineering

Design, System, Application Statement

Controlling the crystallization of water through synthetic systems is a grand challenge with implications from cryopreservation of biologics to the efficiency of wind turbines. Through confinement, the phase behavior and dynamics of water can be altered to provide insights into lengthscales and interactions that are important to manipulating and controlling ice formation. Here, we describe a simple hydrogel system based on an amphiphilic statistical copolymer with crystalline hydrophobic segments that act as effective crosslinks. Through control of the crystallization of these hydrophobic crosslinks through a zone annealing approach, the nanostructure of the hydrogel can be systematically controlled. Small, sub nm scale changes in the nanostructure can dramatically alter the ability of water to crystallize within these hydrogels. This process approach to manipulate the nanostructure in a readily controllable manner provides new opportunities to locally control the crystallization of water with hydrogels.

ARTICLE

Kinetically Controlled Morphology in Copolymer-based Hydrogels Crosslinked by Crystalline Nanodomains Determines Efficacy of Ice Inhibition

Received 00th January 20xx,
Accepted 00th January 20xx

DOI: 10.1039/x0xx00000x

Pablo I. Sepulveda-Medina,[a] Chao Wang,[a,†] Ruipeng Li,[b] Masafumi Fukuto,[b] R.A. Weiss,[a] and Bryan D. Vogt [a,†,*]

Nature uses protein structure to manipulate the properties of water by altering its local environment, but subtle changes in these structures can dramatically influence function. Here, a simple synthetic analog is demonstrated, a statistical copolymer of hydroxyethyl acrylate and n-octadecyl acrylate (HEA-ODA) with 21.3 mol% ODA, to generate hydrogels. The crystallization of the ODA, whose nanodomains act as effective crosslinks, provides a simple route to manipulate the structure through zone annealing without significantly altering the swelling ratio (1.38 to 1.22) for these hydrogels. Despite the identical average composition, changes in the nanostructure induced by zone annealing leads to significant differences in the inhibition of water crystallization within the hydrogels under supercooled conditions with the unfrozen water fraction varying between nearly 60 and 99%. Decreasing the average spacing between crystalline nanodomains leads to increased efficacy of the ice inhibition. However, the morphological details appear to be important as the average number of water molecules confined in a hypothetical square lattice based on the average interdomain spacing and average ODA nanodomain size does not appear to directly scale with the antifreeze capabilities. These results demonstrate control of water crystallization at supercooled temperatures within hydrogels without fluorinated hydrophobic moieties through manipulation of the nanostructure to confine the water.

Introduction

Water is ubiquitous and critical to life as we know it.[1, 2] However despite its relatively simple chemistry,[3] water has fascinated scientists for decades with its complex phase diagram and anomalous properties.[4-8] Confinement of water within nanoporous materials[9-11] can alter the phase diagram and allows for new insights into how changes in the local structure of water influences its properties. For example, sufficiently small water clusters are unable to crystallize,[12] which provide a route to fundamentally understand amorphous water at supercooled temperatures in what is commonly referred to as "no man's land".[13] One aspect associated with water at such small size scale is the prevalence of interfaces that alter the structure of water and its properties.[14-16] Nature has used these subtle alterations in interactions to evolve proteins that allow life to survive in cold environments through prevention of the growth of large ice crystals detrimental to cell viability.[17-20] Much work has gone into the understanding the origins of these antifreeze functions and development of synthetic analogs.[21-24] These materials primarily function to limit the growth of ice crystals by preferentially binding to the surface of nuclei.[19]

In biological settings, proteins can alter the local structure of water through precise arrangement of residues to provide functionality.[25] Water locally in hydrophobic environments exhibits stronger hydrogen bonding,[26] which provides locally more ice-like structure in water near a hydrophobic molecule or protein residue. The role of the local environment hydrophobicity has been examined for water confined in porous materials with different framework chemistries to understand the dynamics of supercooled water.[27-30] Water near a hydrophilic interface exhibits reduced dynamics from the interactions of water with this immobile (at time scales associated with water dynamics) surface,[30] but the melting/freezing of water within the pores was independent of the surface chemistry.[29] Much of the work on water in confinement has focused on supercooled water and amorphous ice as control of ice formation is critical to a wide variety of applications from food[31] to green energy[32] to medicine.[24]

Anti-ice materials have typically been designed around antifreeze proteins[18, 19, 33] to alter the crystal growth or nanoporous inorganic materials[34, 35] to limit nucleation. There are possibilities for soft materials in the form of hydrogels[36-38]

[a] Department of Polymer Engineering, University of Akron, Akron, OH 44325 USA
[b] National Synchrotron Light Source II, Brookhaven National Laboratory, Upton, USA
† Present address: Department of Chemical and Biomolecular Engineering, University of Delaware, Newark, Delaware 19716, USA (C.W.), Department of Chemical Engineering, The Pennsylvania State University, University Park, PA 16802-4400 (B.D.V.).
* Corresponding author: bdv5051@psu.edu (B.D.V.)
Electronic Supplementary Information (ESI) available: ^{1}H NMR of copolymer, temperature gradient for zone annealing, contrast variation SANS, DSC thermograms, SAXS patterns on cooling, and azimuthal dependent scattering of zone annealed hydrogels. See DOI: 10.1039/x0xx00000x

or concentrated polymer solutions[39, 40] to potentially act in both routes (reduce growth and limit nucleation) through the selection of polymeric components. The expansion of water on freezing has been used historically as a route to control structuring within hydrogels,[41-45] but some investigations have noted different states of water within the hydrogels.[46-48] Bound water to the polymer tends to be resistant to crystallization,[49] but this tends to be a minority of the water within the hydrogel so these conventional covalently crosslinked hydrogels are not particularly effective for supressing ice. Recent work has used hydroxyl group density to modulate heterogeneous ice nucleation of poly(vinyl alcohol) through thermally annealing to alter the hydroxyl groups primarily through condensation-based crosslinking.[50] Decreasing the hydroxyl group density increases the ice nucleation temperature.[50] These nature inspired, anti-icing materials have potential in a wide range of applications.[51]

Physical crosslinks that have been widely examined in hydrogels to provide energy dissipation mechanisms to improve their toughness[52, 53] should act to decrease the overall density of hydroxyl groups and adversely influence the bound interfacial water. However, hydrophobically modified polymers that include fluorinated segments tend to assemble into nanoscale domains in hydrogels with sizes[54] comparable to those in porous inorganic materials that exhibit confinement based changes in the properties of water.[34] For hydrogels from copolymers of dimethyl acrylamide (DMA) and 2-(N-ethylperfluorooctane sulfonamido)ethyl acrylate (FOSA), there is a suppression in ice formation as the spacing of the aqueous phase between the FOSA aggregates decreases, but nearly 50% of the water still crystallizes on cooling to cryogenic temperatures.[55] The DMA exhibits relatively weak hydrogen bonding for a water soluble polymer and does not look like polymers that have been shown to be effective for antifreeze applications that tend to include hydroxyl groups.[23] This mechanism is distinct from interfacial bound water that has also been used to influence ice nucleation.[50] Changing the hydrophilic monomer in these physically crosslinked hydrogels to hydroxyethyl acrylate (HEA) provides a monomer chemically more similar to poly(vinyl alcohol), which has been demonstrated to be an effective synthetic analogue for antifreeze proteins.[23] These hydrogels exhibit a marked improvement in their ability to inhibit ice crystallization with > 97% of the water remaining amorphous on cooling down to 128K and slow reheating[56] when the number of water molecules confined between the perfluorinated hydrophobic aggregates was less than 300, which is consistent with spectroscopic studies for the minimum cluster size to obtain signatures of ice.[12] However, the swelling ratio decreases as the concentration of non-freezing water increases, so there are some questions if the antifreeze efficacy is associated with the total water present.

Here we seek to decouple the water content and the structure of the hydrogels through kinetically controlled assembly of the hydrophobic crosslinks in the hydrogels. Additionally, prior work focused on perfluorinated physical crosslinks due to their enhanced hydrophobicity that leads to more effective crosslinks in the hydrogels, but there are concerns regarding cost as well as the environmental and health impact of these fluorinated polymers.[57] To address both of these issues, an alternative hydrophobic crosslinker, octadecyl acrylate (ODA), was copolymerized with HEA to produce hydrogels that were physically crosslinked by ODA crystalline domains. As the size of the ODA crystals can be altered by the details of the crystallization, this provides a simple route to change the morphology without changes in composition or chemistry. To produce a wide diversity in the structure, rotational zone annealing[58] was employed to produce well defined crystallization conditions. These structural differences lead to substantial differences in the efficacy of ice crystallization within these hydrogels at low temperatures. These results demonstrate that (1) perfluorinated hydrophobic crosslinks are not required to inhibit ice crystallization and (2) the size of the water domains within the hydrogel is the controlling factor for high efficacy in preventing water from crystallizing within hydrogels. These concepts may find applications for improved materials as sealants or adhesives for buildings or equipment that are exposed to environmental conditions where the seal could break or fatigue due to the sorption of water and its subsequent crystallization within the material.

Experimental section

Materials.

Hydroxyethyl acrylate (HEA) and n-octadecyl acrylate (ODA) were purchased from Scientific Polymer Products, Inc. (Ontario, NY). Alumina (10% slurry), 2,2'-Azobis(2-methylpropionitrile) (AIBN), 1,4-dioxane (≥ 99.0%), Methanol (≥ 99.8%), N,N-Dimethylformamide (DMF) (≥ 99.8%) and diethyl ether (> 99.7%) were obtained from Sigma Aldrich. Deuterated chloroform ($CDCl_3$) was purchased from Cambridge Isotope, Inc. The inhibitors in the HEA were removed using an aluminium oxide column. The ODA and AIBN were recrystallized in methanol.

An amphiphilic copolymer of HEA and ODA was synthesized by free radical polymerization at 333 K under N_2 atmosphere. The HEA (5.88 g) and ODA (4.11 g) monomers were first dissolved at 15 wt% in 1,4-dioxane (56.6 g). This solution was sparged with N_2 for 30 min under continuous stirring with a Teflon magnetic stir bar. The sparged solution was placed on a pre-heated hotplate at 333K and 8.28 mg AIBN dissolved in 56.66 g 1,4-dioxane was added to the flask to initiate the polymerization. The reaction was terminated after 24 h by cooling to room temperature and exposure to air. The copolymer was precipitated in cold diethyl ether, collected by vacuum filtration, and dried under vacuum at 333 K for 48 h. The chemical structure of the copolymer is shown in Figure 1A. The composition of the copolymer was determined to be 21.3 mol% ODA by ^{1}H NMR (Varian Mercury-300 NMR) using $CDCl_3$ as the solvent as shown in Figure S1. Information about the molecular

weight was determined by size exclusion chromatography (SEC, HLC-8320GPC EcoSec) by dissolution of the HEA-ODA copolymer at 7mg/ml in DMF. In order to dissolve the copolymer, the solution was heated at 323 K for 5h to disrupt the ODA crystals. The solution was filtered (0.2 μm PVDF) prior to injection in the column. Figure S1 shows the SEC trace obtained from this solution in DMF. It should be noted that the SEC operates at ambient temperature and uses an RI detector and TSKgel G4000 Hhr X2 polystyrene column. The molecular mass is reported relative to polystyrene.

The copolymer was compression molded into sheets approximately 0.5mm thick using a vacuum molding machine (Technical Machine Products). The molding conditions were either 333 K or 388K for 30 min to melt the copolymer, followed by pressing at 35 tons for 30 min under a pressure of 100 kPa. The sample was removed from the press and then allowed to cool to ambient temperature.

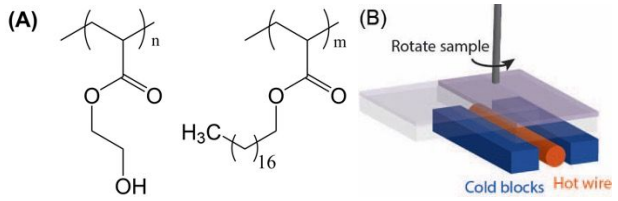

Figure 1. (A) Chemical formula for HEA and ODA that comprises the copolymer. The copolymer contains 21.3 mol% ODA and 78.7 mol% HEA. (B) Schematic of zone annealing setup used to control the nanostructure of the hydrogel.

Zone annealing.

Further control of the nanostructure of the HEA-ODA copolymer was afforded through rotational zone annealing (RZA)[58, 59] to provide a library of different crystallization rates for the ODA. This methodology is a high throughput analogue of traditional zone refinement for metallurgy.[60] The same setup as previously described for RZA was used to produce a sharp temperature gradient using a hot wire between two cooling blocks as illustrated schematically in Figure 1B.[58, 59] The compression molded (at 388K) copolymer sheet (0.25 mm thick) was sandwiched between PTFE sheets to minimize water adsorption into the copolymer film The temperature gradient was measured using an IR camera (FLIR TG165) as shown in Figure S2. The maximum surface temperature during RZA was 384 K with cold blocks held at 304 K. The copolymer sheet on the quartz slide was translated through the temperature gradient using a T-Cube DC Servo Controller with a CR1-Z7 rotating stage. The center of the axis of rotation was 15 mm from one end of the quartz substrate and the quartz slide was rotated 180° from an initial perpendicular orientation relative to the hot wire. The cooled copolymer was then separated from the PTFE to obtain a free standing sheet.

Characterization.

The processed copolymer sheets were swollen in an excess of Milli-Q water to equilibrium to obtain the hydrogels. The copolymer sheets were allowed to swell for more than 96 h for equilibration. These equilibrium swollen hydrogels were then characterized as a function of temperature.

The thermal properties of the hydrogels were assessed using differential scanning calorimetry (DSC, Perkin Elmer DSC 8500 and TA DSC Q 200). A small piece of the hydrogel (0.8-6.2 mg) was hermetically sealed in an aluminium pan and then thermograms on cooling and heating at 2K/min were obtained from 298.5 K to 203 K. To understand any irreversible changes that occurred due to ice, the same heating and cooling cycle was repeated 2-3 times. The unfrozen water fraction in the hydrogels was determined from the heating thermogram. Based on the enthalpy associated with the melting of ice from the thermogram and the known enthalpy of fusion for hexagonal ice, I_h (334 J/g), the mass of ice that melted was determined and compared to the known mass of water in the hydrogel to calculate the unfrozen water fraction.

To better understand the structure of these hydrogels and to confirm crystallization of the water, a combination of small angle X-Ray scattering (SAXS) and wide-angle X-Ray scattering (WAXS) were measured at the 11-BM CMS beamline (National Synchrotron Light Source II, Brookhaven National Laboratory, Upton NY). The 2D SAXS and WAXS patterns were obtained simultaneously using an energy of 13.5keV (λ = 0.0918 nm) with exposures of 10 s on area detectors, Dectris Pilatus 2M (pixel size = 172 μm × 172 μm) and Photonic Science ImageStar (pixel size = 101.7 μm × 101.7 μm) for SAXS and WAXS, respectively. The sample-to-detector distance was 2 m for SAXS and 0.231 m for WAXS. These data were corrected for background and masked to eliminate hot spots on the detector. The corrected data were then circularly averaged to obtain 1-D scattering/diffraction patterns using the Nika package in Igor Pro 6.37.[61] A Linkam TST350 tensile stage with ≈0.10 mm thick Kapton film (DuPont) windows was used to control the temperature between 298 K and 128 K for the scattering experiments. To minimize ice formation on the outside of the Kapton windows, dry nitrogen was blown across the windows.

To complement the SAXS measurements, small angle neutron scattering (SANS) was also performed with contrast variation to better understand the nanostructure of the hydrogels. The SAN measurements were performed on the NGB 30m beam line, at the Center for Neutron Research (NCNR), National Institute and Standards of Technology (NIST), Gaithersburg, MD. For SANS measurements, two different mixtures of H_2O and D_2O (73:27, 87:13 , and pure D_2O were used to equilibrate the copolymer to provide different contrasts to selectively probe different parts of the hydrogel structure. Excess solvent (H_2O:D_2O) was placed on top of the sample to prevent deswelling during the measurements. A neutron wavelength of λ = 0.6 nm with a wavelength spread Δλ/λ of 14% and a beam diameter of 1.91 cm was used for all measurements. To obtain a broad *q* range, three sample to detector distances were used: 1.33 m (with 7 neutron guides), 4.00 m (with 5 neutron guides), and 13.2 m (with 1 neutron guide).

Both the SAXS and SANS data were fit using the unified model developed by Beaucage[62] due to its ability to describe a wide variety of correlated systems and prior success in fitting the scattering of other amphiphilic copolymer hydrogels.[63] The general form of this model is:

$$I(q) = \sum_{i=1}^{n} \frac{(G_i exp\left(\frac{-q^2 R_{g,i}^2}{3}\right) + B_i\left(q_i^*\right)^{-P_i})}{1 + p_i \theta_i(q)} + bkg$$

where F_B is the optional flat background, n is the number of structural levels where G_i is the exponential prefactor for level i, $R_{g,i}$ is the radius of gyration, B_i is the prorod constant that is related to the specific surface area of the scatters of that level, P_i is the Porod exponent, and p_i is the packing factor. The characteristic momentum transfer vector, q^*, is:

$$q^* = \frac{q}{\left[erf\left(\frac{kqR_g}{6^{1/2}}\right)\right]^3}$$

The constant k is associated with the low-q power law limit and assumed to be unity in this case.[62]

$$\theta_i = 3\frac{\sin q\varsigma - q\varsigma\cos q\varsigma}{(q\varsigma)^3}$$

where ζ is the correlation length between structure units.

The Beaucage model was used to fit the Guinier and Porod regions of the SAXS and SANS profiles of the hydrogels. Shape information about the ODA aggerate was included in a size distribution model that includes information from the intermediate and low q region of the scattering profile. These models were implemented within the Irena macro.[64] The size distribution model,[65] which uses the Maximum Entropy method for SAS analysis,[66] has the general form of:

$$I(Q) = \sum_k |\Delta_{\rho k}|^2 S_k(Q) \sum_{ik} |F_k(D,Q_{ik}|^2 V_k(D_{ik}) f_k(D_{ik}) \Delta D_{ik}$$

where $\Delta_{\rho k}$ is the contrast in the system, $S_k(Q)$ is the structure factor, $F(D,Q)$ is the form factor, $V(D)$ is the volume of the particle, $f(D)$ is the volume size distribution and $N(D)$ is the total number size distribution, i is the number of bins of the size distribution, ΔD is the width of the bins, and k is the different populations; where each population has its own i.[62] $N(D)$ is related to $f(D)$:

$$f(D) = V(D)N(D) = V(D)N_{\square}\Psi(D)$$

where $V(D)$ is the volume of the particle, $N_{\square}$ is the total number of scattered particles, and $\Psi(D)$ is the probability of a scatter of size D.[62] The distribution of the particles, which correspond to the ODA aggregates was assumed to be Gaussian. These ODA aggregates can be described as hard spheres to fit the peak in the scattering with the structure factor, which describes the interdomain spacing between ODA aggregates in the network.

Results and discussion

To demonstrate that the crystallization of the ODA can influence the ice inhibition properties in this hydrogel, HEA-ODA copolymer (21.3 mol% ODA) films were compression molded under two conditions (333K or 388K), passively cooled to ambient temperature, and subsequently swollen to equilibrium in H_2O. The swelling ratio, S, for these two processing conditions were 1.38 and 1.39, respectively; (where S is defined as mass of the swollen hydrogel divided by the mass of the hydrogel in its dry state). Figure 2 illustrates that although S is statistically the same for both samples, the nanostructure and low temperature thermal properties of the two hydrogels were very different. Figure 2A compares the DSC cooling thermograms for multiple cooling cycles for the hydrogels prepared from copolymer sheet compression molded at different temperatures conditions for multiple cooling cycles. In both cases, there are exothermic peaks near 270K, 249 K and 220K that are attributed to the crystallization of water within the hydrogels. The presence of two distinct peaks in the thermograms is consistent with multiple states of water within the hydrogel as has been previously been reported.[46] The crystallization exotherm near 249K is much larger for the hydrogel that was originally compression molded at the higher temperature, which indicates more ice was formed for this hydrogel even though the water content and the copolymer composition used to form these two hydrogels were identical.

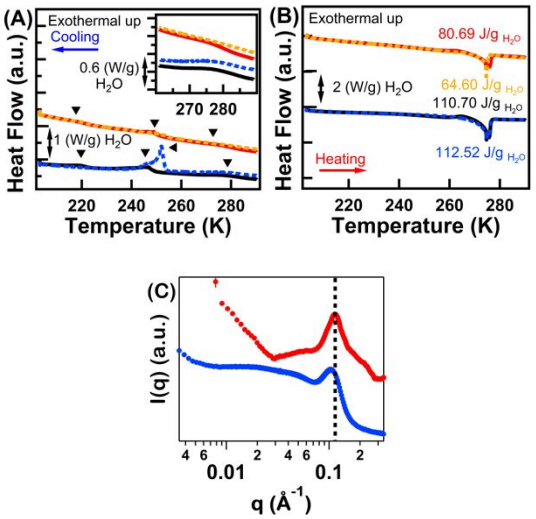

Figure 2. DSC thermograms at 2K/min for HEA-ODA hydrogel on (A) cooling and (B) heating when copolymer was compression molded at 333K (1st cycle red, 2nd cycle yellow) and 383K (1st cycle black, 2nd cycle blue). The exotherms associated with the crystallization of water are denoted by ▼ in (A), while the integrated enthalpy associated with melting ice is provided in (B) on the basis of mass of water in the hydrogel. (C) 1D SAXS profile (red) for hydrogels when copolymer was compression molded at 333K and 1D SANS profile in D_2O (blue) for hydrogels when copolymer was compression molded at 383K prior to freeze-thaw cycling.

Figure 2A also shows that upon re-heating the hydrogel prepared from the film molded at 333K to 298.15 K and then re-cooling to 203K, whereas there was a large crystallization exotherm that appeared near 252K that appears on the second

cooling thermogram for the hydrogel molded at 388K. This difference suggests that the water freezing in the hydrogel processed at the higher temperature may have damaged the sample due to water expansion upon freezing, allowing additional water to crystallize.

Figure 2B shows that for each hydrogel, the heating thermogram shows only a single melting endotherm near 273K. Integration of this endotherm provides the heat of fusion required to melt the ice that had formed within the hydrogels. When the copolymer is processed into a sheet at 333K, 21.8 wt% of the water within the hydrogel was frozen on the second heating cycle, assuming hexagonal ice that is consistent with the melting temperature. For the hydrogel formed from the copolymer molded at the higher temperature, 33.7 wt% of the water within the hydrogel froze in the second heating cycle. Although annealing has been shown to alter freezing of poly(vinyl alcohol) hydrogels through irreversible chemical changes,[50] re-molding of the copolymer does not change the antifreeze performance (as long as the same temperature/cooling is employed) or its equilibrium hydration, which indicates a different mechanism at work where the hydroxyl groups are not reacted during the annealing.

These results of a limited frozen water fraction for the hydrogels from the HEA-ODA copolymer is consistent with a previous report of HEA-fluoroacrylate (HEA-FOSM) hydrogels,[56] but changes in the unfrozen water fraction were realized by changing the FOSM concentration in the copolymer previously , while in the present study, changes in the non-freezing water concentration were achieved by changing the microstructure of the copolymer film. The data shown here indicate that ice inhibition in hydrophobically modified hydrogels does not require a fluorine-containing hydrophobic monomer. Ice inhibition can also be accomplished with a hydrocarbon hydrophobic group. Further, in addition to controlling the amount of non-freezing water in the hydrogel by varying the concentration of the hydrophobic species in the copolymer, varying the processing of the copolymer film precursor to the hydrogel provides another degree of freedom for tailoring the amount of non-freezing water achieved in the hydrogel. For the latter approach, the changes in the microstructure appear to provide the means to change the fraction of non-freezing water.

To understand the origins of these differences in non-freezing water content, the structure of these hydrogels prior to cooling were examined with small angle scattering. Figure 2C illustrates that there are indeed differences at the nanoscale in the structure of these hydrogels. The scattering patterns for both hydrogels exhibit an upturn at low *q*, which is typically observed for hydrogels associated with large scale density fluctuations and a peak at higher *q* that is attributed to the nanostructure associated with the hydrophobic aggregates that comprise the physical crosslinks in these hydrogels. Due to the large hydrogen content of the ODA, it is not possible to uniquely identify the nanostructure of the hydrophobic crosslinks in the hydrogels through contrast variation SANS as a result of the large incoherent scattering when the aqueous phase is matched to ODA (Figure S3). Hydrogels from copolymers with perfluorinated comonomers exhibit a core-shell structure for the hydrophobic aggregates.[54, 67] The scattering data obtained from SAXS and SANS using D_2O in these hydrogels generally provide the same information about the structure due to the origins of the x-ray and neutron contrasts, so we interpret the shift in the peak to lower *q* when the copolymer was compression molded at a higher temperature to an increase in the spacing between the ODA domains. This larger interdomain spacing effectively decreases the degree of water confinement within the hydrogel if the size of the ODA nanodomains are constant. This change in water confinement is consistent with the high fraction of the water in this hydrogel freezing. The difference in the nanostructure with processing is attributed to the sensitivity of the crystallization of the ODA to the temperature and cooling rates used to form the copolymer films.

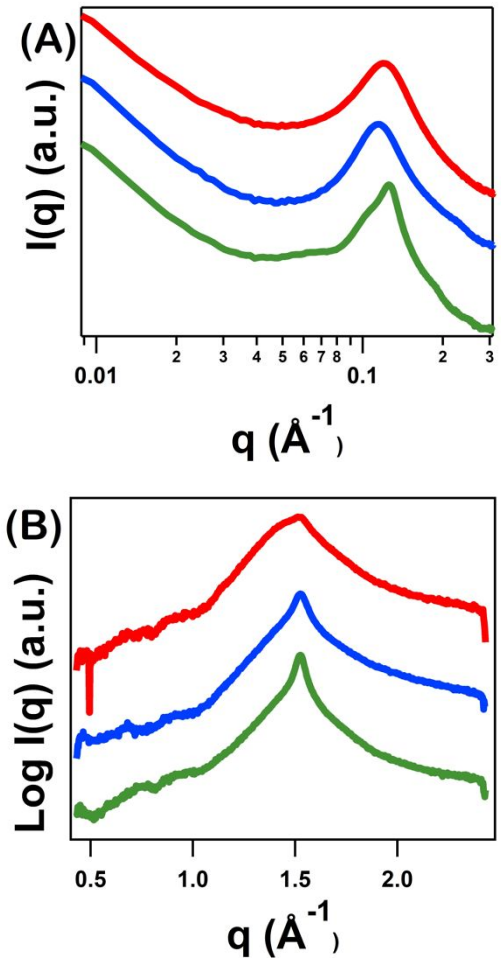

Figure 3. 1D (A) SAXS and (B) WAXS profiles for a single hydrogel that was subjected to a gradient in zone annealing velocities where the scattering was measured at locations corresponding to zone annealing velocities of (red) 46.5 μm/s, (blue) 94.9 μm/s, and (green) 162.1 μm/s. The measurements were performed at 290.6 K. Zone annealing provides a simple route to systematically change the morphology of these hydrogels.

To more precisely control the nanostructure in these hydrogels and to determine how this structure is related to the antifreeze properties, a high throughput zone annealing approach[58] was used to manipulate the crystallization conditions in a controlled manner as illustrated in Figure 1B. Figure 3 illustrates the SAXS and WAXS profiles obtained from locations on the same hydrogel that were subjected to different zone annealing velocities. At the lowest velocity measured, the correlation peak associated with the self-assembled nanostructure of the copolymer (Figure 3A) occurs at higher *q* than either of the hydrogels in Figure 2. As the zone annealing velocity increased from 46 to 162 μm/s, the scattering peak first shifted to lower *q* indicating that the average interdomain spacing of the nanostructure increased, but then moved to higher *q*, indicating a decrease in the nanodomain spacing. Scattering profiles for additional zone annealing conditions are shown in Figure S4. A maximum in the nanostructure spacing occurs when processing at a velocity of 94.9 μm/s. The interdomain spacing obtained at the lowest and highest zone annealing velocities examined was similar.

Figure 3B illustrates the WAXS profiles for these hydrogels at ambient temperature. The broad diffraction peak around q = 1.5 $Å^{-1}$ is typical of the crystal structure of octadecyl acrylate in a random copolymer.[68] At the slowest zone annealing velocity (46.5 μm/s), the diffraction peak is broad and asymmetric with the scattered intensity broadened more towards lower *q*. This suggests that that the lamellae thickness is larger under this slow zone annealing. As the zone annealing velocity is increased, the diffraction peak associated with the ODA in the hydrogel sharpens. This sharper peak could either be associated with more uniform crystal dimensions or larger crystal size (as described by the Scherrer equation). The 2D diffraction patterns are all isotropic rings and thus there is no evidence of alignment of the crystals at the molecular level with zone annealing in these copolymers. However, the combination of SAXS and WAXS illustrates that the nanostructure of the ODA can be readily manipulated using zone annealing.

In order to understand how these differences in the nanostructure influence the efficacy of these hydrogels in inhibiting water crystallization down to cryogenic temperatures, select slices were removed from the hydrogel to perform DSC and *in-situ* SAXS/WAXS on cooling/heating. Figure 4 illustrates the DSC thermograms on heating and cooling for 3 different zone annealing velocities that range the gamut examined. Additional thermograms for these hydrogels are shown in Figure S5. At the slowest velocity (Figure 4A), no clear exotherm peaks on cooling nor an endotherm peak associated with melting near 273K on heating are observed in the thermograms. This indicates that this morphology can effectively prevent ice from crystallizing.

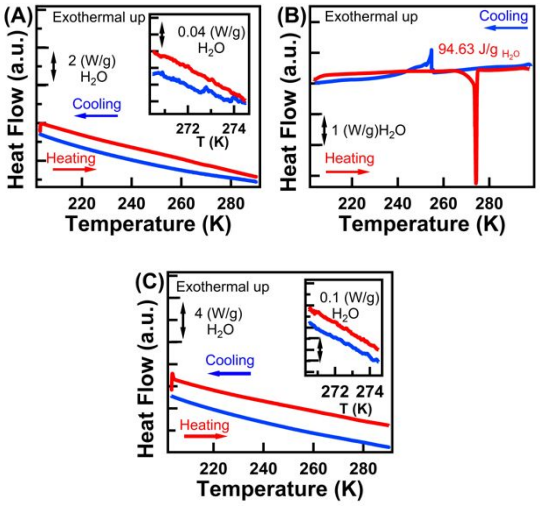

Figure 4. Thermograms on 2nd heating (red) / cooling (blue) for HEA-ODA hydrogels that were zone annealed at (A) 46.5 μm/s, (B) 94.9 μm/s, and (C) 162.1 μm/s. All measurements were performed at 2 K/min. Insets in plots show the region between 270K and 275K on heating to better illustrate the absence of endotherms associated with melting.

The swelling ratio associated with this section of the hydrogel (*S* = 1.36), which is similar to that for the compression molded samples without zone annealing, so the only difference is the arrangement of the hydrophobic ODA within the hydrogel. Even when considering the noise in the DSC data, > 99 % of the water within the hydrogel remains unfrozen on cooling to 200K. When the hydrogel was fabricated with an intermediate velocity (94.9 μm/s, Figure 4B, *S* = 1.33), the melting of ice can be readily observed in the thermogram on heating. Integration of this endotherm leads to the conclusion that 31% of the water within this hydrogel crystallized on cooling and melted on heating. As shown in Figure 4C (*S* = 1.28), the ice inhibition in the hydrogel improves again when a higher zone annealing rate is used (162.1 μm/s) with> 99 % of the water within the hydrogel remaining unfrozen on cooling to 200K. These observations are consistent with the expectation that smaller spaces between the hydrophobic crosslinks will lead to improved antifreeze performance[56] as the confinement size approaches the critical size for ice to form in water clusters.[12]

To confirm the differences in ice inhibition for these hydrogels as well as understand how the structure changes at low temperatures, simultaneous SAXS and WAXS measurements were performance on these three hydrogels as the temperature was decreased down to 133K. To quantify the changes in the nanostructure, the SAXS profiles were fit using the unified model as shown in Figure 5. This model can describe the data for all three hydrogels well through all temperatures examined. Fits at additional temperatures are shown in Figures S6 (46.5 μm/s), S7 (94.9 μm/s) and S8 (162.1 μm/s). Despite the directionality of zone annealing, the scattering profiles remained relatively isotropic (insets in Figure 5). Subtle differences in the nanostructure that can influence the antifreeze capabilities of these hydrogels can be thus identified by SAXS.

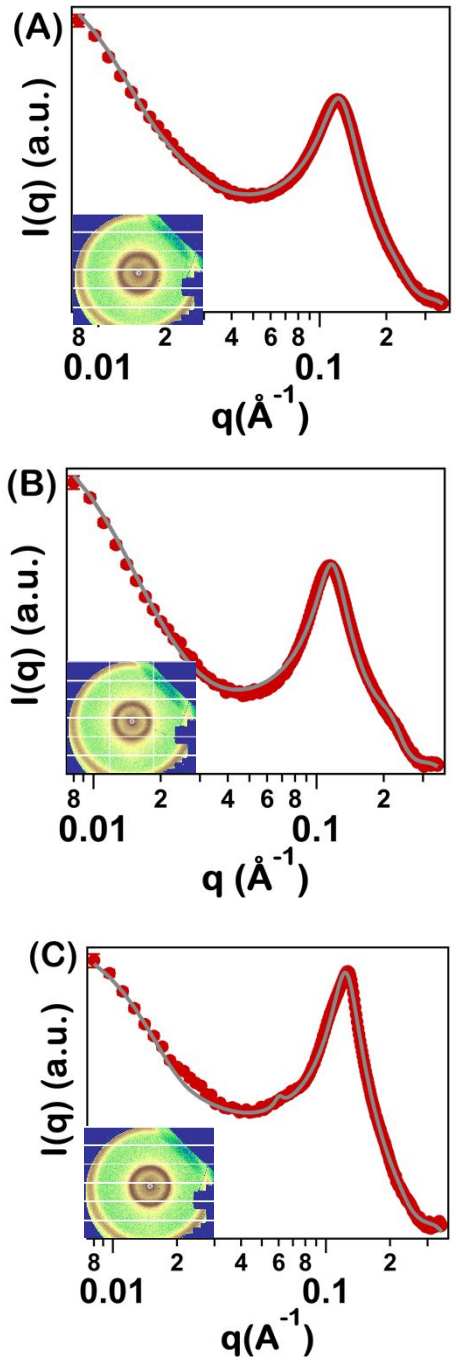

Figure 5. Azimuthally averaged 1D SAXS profiles at 298 K for the HEA-ODA hydrogels that were zone annealed at (A) 46.5 μm/s, (B) 94.9 μm/s, and (C) 162.1 μm/s. The 2D SAXS patterns are shown in the insets. The grey line is the fit of the scattering data

From the unified model, both the spacing between nanodomains and the size of the nanodomains can be determined from the scattering data. As we hypothesize that the zone annealing process alters the crystalline structure of the ODA, it is instructive to examine the distribution in sizes of these nanodomains that can be extracted from the scattering data. Figure 6 illustrates how the size of the ODA nanodomains evolve on cooling as determined from the SAXS measurements. For the hydrogel fabricated by zone annealing at 46.5 μm/s (Figure 6A), there is a relatively narrow distribution of ODA sizes that appears Gaussian. On cooling to 270K, there is a decrease in the size of the domains, but limited changes in the size distribution are found for temperatures below 243K. This limited change in dimensions is consistent with limited crystallization of water within these hydrogels.

Conversely for the hydrogel where significantly more water crystallizes, a bimodal distribution of sizes was obtained from the fits of the SAXS data (Figure 6B) at low temperatures. The smaller size exhibits a larger change on cooling than for the previously described hydrogel. A small fraction of the domains in this case are much larger (inset in Figure 6B). The fraction of this larger size grows as the hydrogel is cooled, which we attribute to the phase separation of the copolymer from the ice with these sizes being the copolymer free of water. As the contrast between water and the copolymer is much greater than that between HEA and ODA, regions that are copolymer rich versus water rich are consistent with this larger size.

At the fast zone annealing rate (Figure 6C), the distribution of nanodomain sizes is initially unimodal with a broad peak centered at 19 Å. On cooling, there is a shift in this broad peak to smaller average size, but the distribution appears to become bimodal with a narrow size distribution arising that is generally within the original size distribution. Although the change in structure is greater than observed for the other hydrogel with high efficacy for ice inhibition (Figure 6A), the size of the nanodomains remain relatively small (<3 nm) unlike the larger size scales that arise for the hydrogel with lower ice inhibition properties (Figure 6B).

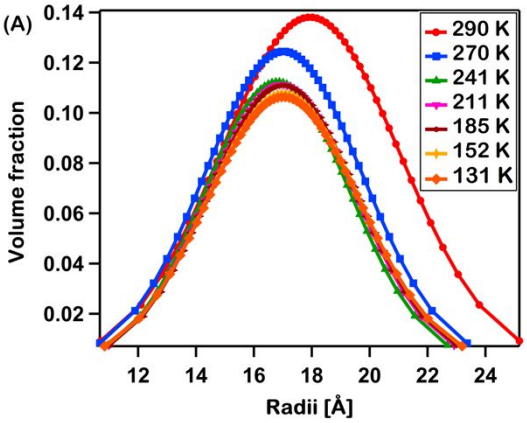

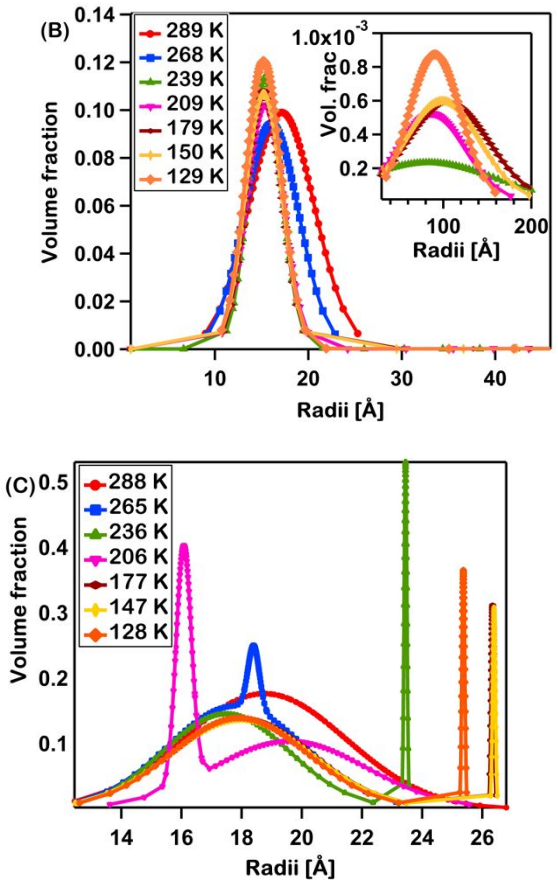

Figure 6. Temperature dependence of the size distribution of the radii of the ODA domains determined from the unified model fits for the HEA-ODA hydrogels processed by zone annealing at (A) 46.5 μm/s, (B) 94.9 μm/s, and (C) 162.1 μm/s. Inset in (B) illustrates the larger scale structures obtained under these conditions.

The crystallization of water within these hydrogels can also be assessed by examination of the temperature dependent WAXS profiles as shown in Figure 7. There is a broad peak in the diffraction profiles at all temperatures examined, which is associated with the crystals of the ODA in the hydrogel. As shown in Figure 7A, additional sharp peaks arise in the WAXS profile for the hydrogel processed by zone annealing at 46.5 μm/s on cooling to low temperatures. To prevent beam damage, the sample is rastered. The measurements at different locations provide insights into heterogeneities in the hydrogels (low *q* upturn in intensity in Figure 5) that lead to difference in the ice inhibition. However in this case, the large spike in the diffraction at 165.15K is attributed to ice forming on the surface of the window. Nitrogen gas is blown over the surface to minimize surface icing during the measurement, but near the edges ice still forms on the outer edges of the surface from the ambient humidity (as shown in the photograph in Figure S9). In general, the diffraction peaks associated with ice remain small as expected from DSC (Figure 4A) for this hydrogel with its excellent ice inhibition properties.

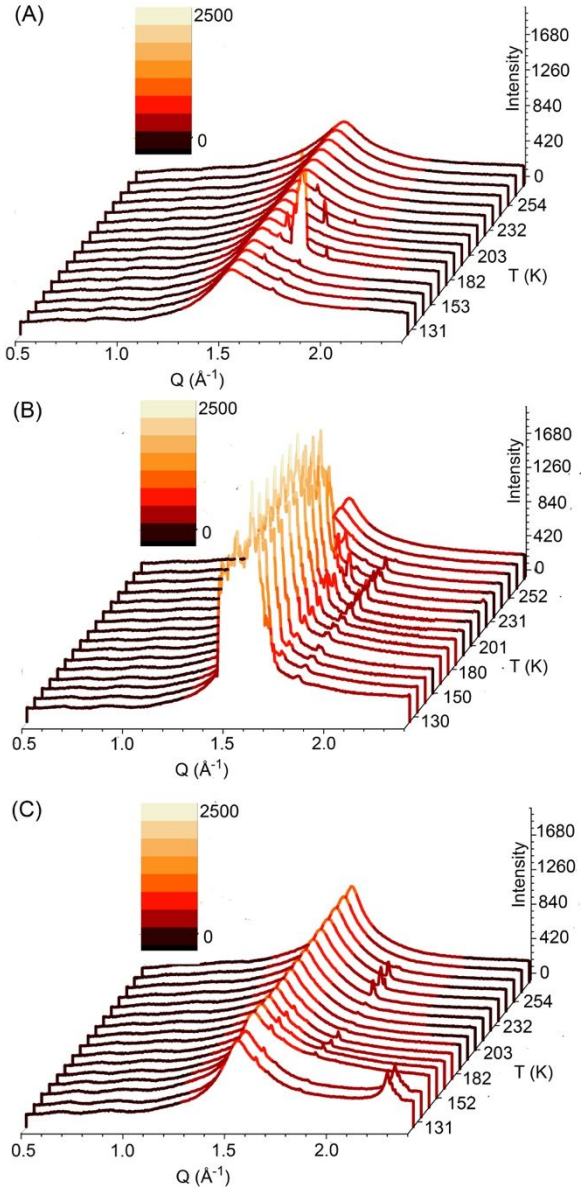

Figure 7. Waterfall plots illustrating the WAXS profiles on cooling from 270.15 K to 128.15 K for the HEA-ODA hydrogels that were zone annealed at (A) 46.5 μm/s, (B) 94.9 μm/s, and (C) 162.1 μm/s.

Conversely, the WAXS profiles show clear evidence of ice within the hydrogel processed by zone annealing at 94.9 μm/s on cooling below 239 K (Figure 4B). The intensity of the diffraction peak of ice grows on further cooling to 209 K and then remains invariant on further cooling. This behavior is consistent with significant water crystallization in this hydrogel. Increasing the zone annealing to 162.1 μm/s leads to only small diffraction peaks associated with the crystallization of water (Figure 4C), which is similar to the WAXS profiles obtained from measurements of the hydrogel at the slowest zone annealing velocity (Figure 4A). These results are consistent with DSC and demonstrates that ice is readily formed when the hydrogels are processed at an intermediate zone annealing velocity. Thus, details of the nanostructure in these hydrogels appear to control the ability of water to crystallize.

To better understand how the nanostructure influences the ability of water to crystalize within these hydrogels, the interdomain spacing, swelling ratio, and the mean size of the ODA domains were used to estimate the number of water molecules (N_w) confined between the domains at 298K (see Table 1) assuming a cubic lattice following the work of Wang *et al*.[56] The temperature dependence of the interdomain spacing and size of the ODA nanodomains are shown in Figure S10. Figure 8 illustrates how the fraction of non-freezing water in the hydrogel depends on N_w. Qualitatively similar to prior results for HEA-FOSM hydrogels,[56] the non-freezing water fraction tends to increase as the calculated N_w decreases for these zone annealed hydrogels. There is, however, a quantitative difference in the dependence of N_w on the non-freezing water fraction between these two hydrogel systems. For the HEA-ODA based hydrogels, the number of water molecules confined between the ODA nanodomains is, in all cases, smaller than the reported cluster sizes where spectral features of ice are not observed under supercooled conditions.[12] This is counter to the HEA-FOSM hydrogel where the cluster size corresponded well with the calculated N_w. This difference may be associated with the nature of the physical crosslinks as the ODA is crystalline. The calculation associated with N_w assumes an isotropic distribution of the physical crosslinks with a single average spacing between these ODA nanodomains that have a single average size. These parameters are determined from the best fit of the SAXS data. However as shown in Figure 6, there is a distribution of sizes for the ODA nanodomains that depends on the processing condition. For a broad size distribution, the number of water molecules confined between the nanodomains will be variable. The smaller nanodomain sizes will increase N_w and this variation may be responsible for the higher fractions of frozen water despite the average size leading to dimensions that would be expected to inhibit water crystallization based on spectroscopic measurements of water clusters.[12]

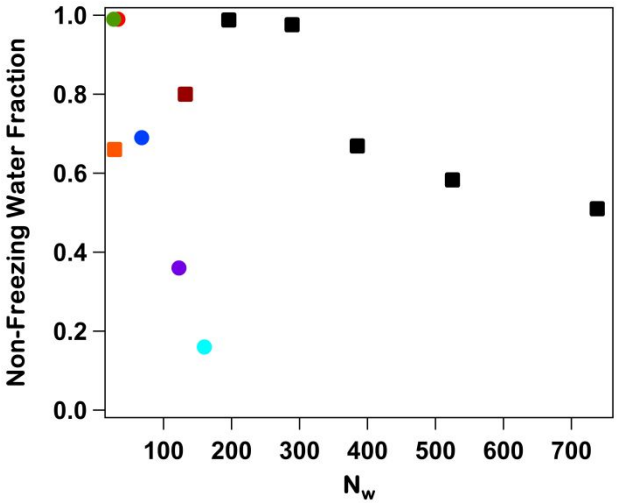

Figure 8. Relationship between N_w and the non-freezing water fraction for HEA-ODA hydrogels that were processed by zone annealing at (●) 46.5 μm/s, (●) 68.0 μm/s, (●) 94.9 μm/s, (●) 121.8 μm/s, and (●) 162.1 μm/s, and melt processed at (■) 333.15 K and (■) 388.15 K. For comparison, (■) HEA-FOSM hydrogels previously reported where the morphology was manipulated by changing the composition of the copolymer.[56] The calculation assumes an isotropic nanostructure with a simple cubic arrangement for the nanodomains.

Based on our prior experience in zone annealing of semicrystalline polymers,[58] there is a potential for anisotropy in the structure from the zone annealing. Examination of the 2D scattering patterns shows that the correlation peak is a circular ring, not an ellipse, so the nanostructure does not appear to be anisotropic. However, examination of scattering at multiple incidence angles shows some modest azimuthal dependence on the scattered intensity associated with the correlation peak (Figure S10). This suggests that there is some difference in the contrast or number density of the nanodomains through the thickness of the zone annealed hydrogels. The zone annealing conditions that lead to the greatest anisotropy in the scattered intensity as shown in Figure S10 appears to be correlated with decreased efficacy in inhibiting ice. This anisotropy in the scattering is suggestive of differences in the local water rich dimensions between in-plane and out-of-plane (relative to the zone annealing process). It is these differences that lead to the differences in antifreeze efficacy based on zone annealing conditions for this hydrogel. This work demonstrates that small subtle differences in the nanostructure can tremendously influence the ability of water to crystallize within these hydrophobically crosslinked hydrogels.

Table 1. Properties of the HEA-ODA hydrogels at 298 K.

Velocity (μm/s)	S	d_c (nm)	$d_{c\text{-}c}$ (nm)	d_{sp} (nm)	N_w
46.5	1.36	3.58	5.23	1.65	32.88
68.0	1.34	3.51	5.63	2.12	122.56
94.9	1.33	3.42	5.60	2.18	67.83
121.8	1.22	3.36	5.59	2.23	160.25
162.1	1.28	3.74	5.36	1.62	26.65

S = swelling ratio. d_c = average nanodomain diameter. $d_{c\text{-}c}$ = average spacing between neighboring nanodomain. d_{sp} = average interdomain spacing; $d_{sp} = d_{c\text{-}c} - d_c$. N_w = number of water molecules in the confined volume.

Conclusions

Hydrogels obtained from hydration of a single copolymer of HEA and ODA exhibit process dependent antifreeze properties. This sensitivity arises from the kinetic control of the nanostructure through the crystallization of the ODA segments that act as physical crosslinks for the hydrogel. Zone annealing was applied to provide systematic control of the crystallization. Interestingly, the largest spacing between ODA domains occurred at intermediate zone annealing velocity. The fraction of water that does not crystallize in these hydrogels as determined from DSC is not correlated with the swelling ratio (water content) that modestly depends on the zone annealing velocity. These conclusions are confirmed by *in-situ* WAXS measurements that corroborate the DSC conclusions on antifreeze performance. The fraction of water that does not freeze within these hydrogels can be controlled from >99% to

<20% based on the processing conditions. Both anisotropy in the scattered intensity associated with the correlations from the ODA nanodomains and the size distribution of the nanodomains appear to be directly related to the anti-ice efficacy with greater efficacy for more uniform and isotropic hydrogels. These results illustrate the ability to dramatically influence the ability of water to crystallize within a hydrophobically-crosslinked hydrogel based on subtle changes to its nanostructure.

Conflicts of interest

There are no conflicts to declare.

Acknowledgements

This work was supported by a grant (CBET-1606685) from the Chemical, Bioengineering, Environmental, and Transport Systems Division of the Directorate for Engineering of the National Science Foundation. The research used the Complex Materials Scattering (CMS/11-BM) beamline, operated by the National Synchrotron Light Source II and the Center for Functional Nanomaterials, which are U.S. Department of Energy (DOE) Office of Science User Facilities operated for the DOE Office of Science by Brookhaven National Laboratory under Contract No. DE-SC0012704. Access to the NGB 30m SANS was provided by the Center for High Resolution Neutron Scattering, a partnership between the National Institute of Standards and Technology and the National Science Foundation under Agreement No. DMR-1508249. We acknowledge the support of the National Institute of Standards and Technology, U.S. Department of Commerce, in providing the neutron research facilities used in this work.

Notes and references

1. O. Mishima and H. E. Stanley, *Nature*, 1998, **396**, 329-335.
2. P. Ball, *Chem. Rev.*, 2008, **108**, 74-108.
3. W. L. Jorgensen, J. Chandrasekhar, J. D. Madura, R. W. Impey and M. L. Klein, *J. Chem. Phys.*, 1983, **79**, 926-935.
4. W. Wagner and A. Pruss, *J. Phys. Chem. Refer. Data*, 2002, **31**, 387-535.
5. D. T. Limmer and D. Chandler, *Proc. Natl. Acad. Sci. USA*, 2014, **111**, 9413-9418.
6. M. M. Koza, B. Geil, K. Winkel, C. Kohler, F. Czeschka, M. Scheuermann, H. Schober and T. Hansen, *Phys. Rev. Lett.*, 2005, **94**, 125506.
7. J. M. Zanotti, M. C. Bellissent-Funel and S. H. Chen, *Europhys. Lett.*, 2005, **71**, 91-97.
8. C. Lobban, J. L. Finney and W. F. Kuhs, *Nature*, 1998, **391**, 268-270.
9. E. Tombari, G. Salvetti, C. Ferrari and G. P. Johari, *J. Chem. Phys.*, 2005, **122**, 104712.
10. K. Koga, H. Tanaka and X. C. Zeng, *Nature*, 2000, **408**, 564-567.
11. D. Takaiwa, I. Hatano, K. Koga and H. Tanaka, *Proc. Natl. Acad. Sci. USA*,, 2008, **105**, 39-43.
12. C. C. Pradzynski, R. M. Forck, T. Zeuch, P. Slavicek and U. Buck, *Science*, 2012, **337**, 1529-1532.
13. E. B. Moore and V. Molineroa, *J. Chem. Phys.*, 2010, **132**, 10.
14. M. R. Harpham, B. M. Ladanyi, N. E. Levinger and K. W. Herwig, *J. Chem. Phys.*, 2004, **121**, 7855-7868.
15. F.-X. Coudert, F. Cailliez, R. Vuilleumier, A. H. Fuchs and A. Boutin, *Faraday Discuss.*, 2009, **141**, 377-398.
16. T. G. Lombardo, N. Giovambattista and P. G. Debenedetti, *Faraday Discuss.*, 2009, **141**, 359-376.
17. B. L. Pentelute, Z. P. Gates, V. Tereshko, J. L. Dashnau, J. M. Vanderkooi, A. A. Kossiakoff and S. B. H. Kent, *J. Am. Chem. Soc.*, 2008, **130**, 9695-9701.
18. F. Sicheri and D. S. C. Yang, *Nature*, 1995, **375**, 427-431.
19. Y. Yeh and R. E. Feeney, *Chem. Rev.*, 1996, **96**, 601-617.
20. L. B. Chen, A. L. DeVries and C. H. C. Cheng, *Proc. Natl. Acad. Sci. USA*, 1997, **94**, 3817-3822.
21. B. Graham, A. E. R. Fayter, J. E. Houston, R. C. Evans and M. I. Gibson, *J. Am. Chem. Soc.*, 2018, **140**, 5682-5685.
22. C. J. Capicciotti, M. Leclere, F. A. Perras, D. L. Bryce, H. Paulin, J. Harden, Y. Liu and R. N. Ben, *Chem. Sci.*, 2012, **3**, 1408-1416.
23. R. C. Deller, M. Vatish, D. A. Mitchell and M. I. Gibson, *Nat. Commun.*, 2014, **5**, 3244.
24. B. Graham, T. L. Bailey, J. R. J. Healey, M. Marcellini, S. Deville and M. I. Gibson, *Angew. Chem.Int. Ed.*, 2017, **56**, 15941-15944.
25. E. A. Vogler, *Adv. Colloid Interface Sci.*, 1998, **74**, 69-117.
26. J. Grdadolnik, F. Merzel and F. Avbelj, *Proc. Natl. Acad. Sci. USA*, 2017, **114**, 322-327.
27. Y. Zhang, K. H. Liu, M. Lagi, D. Liu, K. C. Littrell, C. Y. Mou and S. H. Chen, *J. Phys. Chem. B*, 2009, **113**, 5007-5010.
28. M. Aso, K. Ito, H. Sugino, K. Yoshida, T. Yamada, O. Yamamuro, S. Inagaki and T. Yamaguchi, *Pure Appl. Chem.*, 2013, **85**, 289-305.
29. K. Morishige, *J. Phys. Chem. C*, 2018, **122**, 5013-5019.
30. C. G. Wiener, Z. Qiang, Y. F. Xia, M. Tyagi and B. D. Vogt, *Phys. Chem. Chem. Phys.*, 2018, **20**, 28019-28025.
31. H. Kiani and D.-W. Sun, *Trends Food Sci. Technol.*, 2011, **22**, 407-426.
32. O. Parent and A. Ilinca, *Cold Regions Sci. Technol.*, 2011, **65**, 88-96.
33. D. E. Mitchell, M. Lilliman, S. G. Spain and M. I. Gibson, *Biomater. Sci.*, 2014, **2**, 1787-1795.
34. R. Bergman and J. Swenson, *Nature*, 2000, **403**, 283-286.
35. T. Yamaguchi, H. Hashi and S. Kittaka, *J. Mol. Liquids*, 2006, **129**, 57-62.
36. G. Paradossi, F. Cavalieri, E. Chiessi and M. T. F. Telling, *J. Phys. Chem. B*, 2003, **107**, 8363-8371.
37. E. Chiessi, F. Cavalieri and G. Paradossi, *J. Phys. Chem. B*, 2005, **109**, 8091-8096.
38. Y. Sekine, T. Ikeda-Fukazawa, M. Aizawa, R. Kobayashi, S. X. Chi, J. A. Fernandez-Baca, H. Yamauchi and H. Fukazawa, *J. Phys. Chem. B*, 2014, **118**, 13453-13457.
39. X. S. Du, D. Seeman, P. L. Dubin and D. A. Hoagland, *Langmuir*, 2015, **31**, 8661-8666.
40. S. Ali and F. A. Bettelheim, *Colloid Polym. Sci.*, 1985, **263**, 396-398.
41. S. Van Vlierberghe, V. Cnudde, P. Dubruel, B. Masschaele, A. Cosijns, I. De Paepe, P. J. S. Jacobs, L. Van Hoorebeke, J.

P. Remon and E. Schacht, *Biomacromolecules*, 2007, **8**, 331-337.
42. V. I. Lozinsky, L. G. Damshkaln, I. N. Kurochkin and Kurochkin, II, *Colloid J.*, 2012, **74**, 319-327.
43. H. Bai, A. Polini, B. Delattre and A. P. Tomsia, *Chem. Mater.*, 2013, **25**, 4551-4556.
44. R. Aston, K. Sewell, T. Klein, G. Lawrie and L. Grondahl, *Eur. Polym. J.*, 2016, **82**, 1-15.
45. H. J. He, M. Y. Liu, J. J. Wei, P. Chen, S. L. Wang and Q. G. Wang, *Adv. Healthcare Mater.*, 2016, **5**, 648-652.
46. W. B. Li, F. Xue and R. S. Cheng, *Polymer*, 2005, **46**, 12026-12031.
47. V. M. Gun'ko, I. N. Savina and S. V. Mikhalovsky, *Gels*, 2017, **3**.
48. K. Ito, K. Yoshida, K. Ujimoto and T. Yamaguchi, *Anal. Sci.*, 2013, **29**, 353-359.
49. T. Nakano and T. Nakaoki, *Polym. J.*, 2011, **43**, 875-880.
50. S. W. Wu, Z. Y. He, J. Zang, S. L. Jin, Z. W. Wang, J. P. Wang, Y. F. Yao and J. J. Wang, *Sci. Adv.*, 2019, **5,** eaat9825.
51. Z. Y. He, K. Liu and J. J. Wang, *Acc.Chem. Res.*, 2018, **51**, 1082-1091.
52. T. L. Sun, T. Kurokawa, S. Kuroda, A. Bin Ihsan, T. Akasaki, K. Sato, M. A. Haque, T. Nakajima and J. P. Gong, *Nat. Mater.*, 2013, **12**, 932-937.
53. D. C. Tuncaboylu, M. Sari, W. Oppermann and O. Okay, *Macromolecules*, 2011, **44**, 4997-5005.
54. J. Tian, T. A. P. Seery, D. L. Ho and R. A. Weiss, *Macromolecules*, 2004, **37**, 10001-10008.
55. C. G. Wiener, M. Tyagi, Y. Liu, R. A. Weiss and B. D. Vogt, *J. Phys. Chem. B*, 2016, **120**, 5543-5552.
56. C. Wang, C. G. Wiener, P. I. Sepulveda-Medina, C. H. Ye, D. S. Simmons, R. P. Li, M. Fukuto, R. A. Weiss and B. D. Vogt, *Chem. Mater.*, 2019, **31**, 135-145.
57. M. F. Rahman, S. Peldszus and W. B. Anderson, *Water Research*, 2014, **50**, 318-340.
58. C. H. Ye, C. Wang, J. Wang, C. G. Wiener, X. H. Xia, S. Z. D. Cheng, R. P. Li, K. G. Yager, M. Fukuto and B. D. Vogt, *Soft Matter*, 2017, **13**, 7074-7084.
59. C. H. Ye, Y. Sun, A. Karim and B. D. Vogt, *Macromolecules*, 2015, **48**, 7567-7573.
60. A. N. Christensen and P. Roehammer, *J. Crystal Growth*, 1977, **38**, 281-283.
61. J. Ilavsky, *J. Appl. Crystallogr.*, 2012, **45**, 324-328.
62. G. Beaucage, *J. Appl. Crystallogr.*, 1996, **29**, 134-146/
63. C. Wang, C. G. Wiener, M. Fukuto, R. P. Li, K. G. Yager, R. A. Weiss and B. D. Vogt, *Soft Matter*, 2019, **15**, 227-236.
64. J. Ilavsky and P. R. Jemian, *J. Appl. Crystallogr.*, 2009, **42**, 347-353.
65. J. A. Potton, G.J. Daniell and B.D. Rainford, *J. Appl. Crystallogr.*, 1988, **21**, 891-897.
66. R. K. Bryan and J. Skilling, Mon. Not. R. Astron. Soc., 1980, 191, 69-79.
67. C. G. Wiener, C. Wang, Y. Liu, R. A. Weiss and B. D. Vogt, *Macromolecules*, 2017, **50**, 1672-1680.
68. A. Matsuda, J. Sato, H. Yasunaga and Y. Osada, *Macromolecules*, 1994, **27**, 7695-7698.

Table of Contents Entry

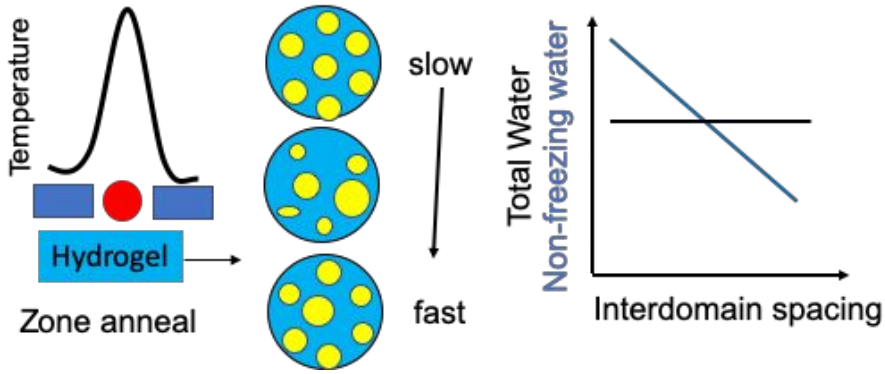

Zone annealing crystalline cross-linked hydrogels manipulates nanostructure that controls anti-icing performance